

Searching for Galaxy Cluster-Scale Strong lenses from the DESI Legacy Imaging Surveys

ZHEJIAN ZHANG,¹ NAN LI,² SHUDE MAO,³ HU ZOU,² ZIZHAO HE,^{4,5,6} MINGXIANG FU,^{7,8} AND SHENZHE CUI^{7,8}

¹*Department of Astronomy, Tsinghua University, Beijing 100084, China*^{*}

²*National Astronomical Observatories, Chinese Academy of Sciences, 20A Datun Road, Chaoyang District, Beijing 100012, China*

³*Department of Astronomy, School of Science, Westlake University, Hangzhou, Zhejiang 310030, China*

⁴*Department of Physics, Nanchang University, Nanchang, 330031, China*

⁵*Center for Relativistic Astrophysics and High Energy Physics, Nanchang University, Nanchang, 330031, China*

⁶*Purple Mountain Observatory, Chinese Academy of Sciences, Nanjing, Jiangsu, 210023, China*

⁷*School of Astronomy and Space Science, University of Chinese Academy of Sciences, Beijing 101408, China*

⁸*National Astronomical Observatories, Chinese Academy of Sciences, Beijing 100101, China*

ABSTRACT

Galaxy cluster-scale strong gravitational lensing systems are rare yet valuable tools for investigating the properties of dark matter and dark energy, as well as providing the opportunity to study the distant universe at flux levels and spatial resolutions that would otherwise be unavailable. Large-scale imaging surveys present unprecedented opportunities to expand the sample of cluster lenses. In this study, we adopt a deep learning-based approach to identify cluster lenses from the DESI Legacy Imaging Surveys, utilizing the catalog of galaxy cluster candidates identified by Zou et al. (2021). Our lens-finder employs a ResNet-18 architecture, trained with mock images of cluster lenses as positives and observational images of cluster scale non-lenses as negatives. We do an iterative operation to increase the completeness of our work, namely adding the found true positive samples back to the training set and training again for several times. Human inspection is conducted to further refine the candidates, categorizing them into grades (A, B, C) according to the significance of the strongly lensed arcs. Reviewing all 540,432 objects in Zou's catalog, we discover 485 high-confidence cluster lens candidates with a cluster M_{500} range of $10^{13.67\sim14.97} M_{\odot}$ and a Brightest Central Galaxy (BCG) redshift range of $0.04 \sim 0.89$. After excluding the lens candidates listed in previous studies, we identify 247 newly discovered cluster lens candidates, including 16 grade A, 90 grade B, and 141 grade C. This catalog of cluster lens candidates is publicly available online^{a)}, and follow-up observations are encouraged to confirm and conduct thorough investigations of these systems.

Keywords: Strong Gravitational Lenses - Galaxy Cluster- Convolutional Neural Network

1. INTRODUCTION

Strong gravitational lensing (SGL) refers to the noticeable distortion of a distant source's image caused by the gravitational field of massive objects located between the observer and the source (Narayan & Bartelmann 1996). This phenomenon produces distinctive features, such as Einstein rings, arcs, or multiple images. Strong gravitational lensing systems serve as a valuable tool for cosmological research, enabling the study of the distribution of mass, particularly dark matter, within lensing objects (e.g. Narayan & White 1988; Treu 2010; Massey et al. 2010; Grillo et al. 2015; Meneghetti et al. 2020). Time-delay measurements between multiple lensed images provide a geometric method to constrain the Hubble constant (e.g. Refsdal 1964; Grogin & Narayan 1996; Suyu et al. 2017; Wong et al. 2020). Additionally, the magnification effect of SGL facilitates the observation of intrinsically faint populations at high redshifts, offering insights into early star formation and galaxy assembly (e.g. Kelly et al. 2018; Welch et al. 2022; Palencia et al. 2024).

^{a)} <https://github.com/zkzdyzg/Galaxy-Cluster-Scale-Strong-lenses-from-the-DESI-Legacy-Imaging-Surveys>

* nan.li@nao.cas.cn

Cluster-scale strong lensing systems, where massive galaxy clusters ($M_{500} \gtrsim 10^{14} M_{\odot}$) act as gravitational lenses, produce distinctive arcs or ring structures, offering numerous scientific opportunities (e.g. Narayan et al. 1984; Kneib et al. 1996; Kneib & Natarajan 2011; Jullo et al. 2007; Richard et al. 2010; Postman et al. 2012; Coe et al. 2019). These systems provide valuable insights into both astrophysical and cosmological aspects. Their sensitivity to gravitational effects enables the mapping the cluster mass distributions (Kneib et al. 1993; Jullo & Kneib 2009; Coe et al. 2012; Jauzac et al. 2015), constraining the properties of dark matter or cosmology (Jullo et al. 2010; Caminha et al. 2016), and probing the mechanisms of cluster formation (Merten et al. 2015). Moreover, the magnification of high redshift background sources enables the study of galaxy formation during the earliest epochs, which extended to the dark age (Kneib et al. 2004; Coe et al. 2013). Furthermore, previous studies demonstrate that light deflection information can constrain cosmological parameters, offering a powerful geometric tool to probe Dark Energy (Jullo et al. 2010).

Galaxy cluster-scale strong lensing systems are, however, rare phenomena (Faure et al. 2008; Oguri 2010). The advent of wide-field sky surveys, such as the Dark Energy Spectroscopic Instrument (DESI) Legacy Imaging Surveys (Dey et al. 2019), the Vera C. Rubin Observatory’s Legacy Survey of Space and Time (LSST) (Ivezić et al. 2019), and Euclid (Euclid Collaboration et al. 2025), has increased the opportunity to discover these rare systems. With the vast amount of data generated, many strong lensing events likely remain undiscovered. However, identifying them is a challenge (Metcalf et al. 2019). Traditional detection pipelines, which rely on visual inspection (Khullar et al. 2021) or parametric morphology filters (e.g., arc length and curvature thresholds) (Lenzen et al. 2004; Horesh et al. 2005; Alard 2006; Seidel & Bartelmann 2007; Xu et al. 2016), scale poorly to such massive data volumes. Manual vetting becomes prohibitively time-intensive, whereas rule-based algorithms suffer from high false-positive rates due to contaminants such as spiral arms, tidal debris, and edge-on galaxies.

Recent advancements in machine learning, particularly in Convolutional Neural Networks (CNNs), have shown remarkable potential for detecting strong gravitational lenses in astronomical imaging data. Trained on large-scale simulations of lensing systems, CNNs are highly effective at identifying subtle morphological features, such as faint arcs or distorted counterimages, which often evade traditional detection algorithms (Jacobs et al. 2019). Early applications of CNN-based classifiers, such as those employed in the Hyper Suprime-Cam Subaru Strategic Program (HSC-SSP) (Jaelani et al. 2024), the Kilo-Degree Survey (KiDS) (Petrillo et al. 2017; Li et al. 2021) and the Dark Energy Spectroscopic Instrument (DESI) Legacy Surveys (Huang et al. 2020; Huang et al. 2021; Storfer et al. 2024), have achieved recall rates of $\geq 90\%$ for galaxy-scale lenses. These methods reduce false positive rates by an order of magnitude compared to rule-based approaches, demonstrating their effectiveness in addressing the challenges of lens discovery in massive datasets.

In this study, we present a CNN-based methodology designed to identify cluster-scale strong gravitational lensing systems within the cluster catalog compiled by Zou et al. (2021) from the DESI Legacy Imaging Surveys. Our method employs an 18-layer ResNet architecture, chosen for its demonstrated effectiveness in extracting features from complex astronomical images, to systematically detect strong lensing signatures within galaxy clusters. To train the model, we generate realistic cluster-scale lensing images using a mock program that combines DESI legacy imaging of real galaxy clusters with synthetic lensed background sources, incorporating variations in mass distribution, redshift, and observational conditions. The initial CNN model, trained on mocked data, is applied to the DESI fields to identify strong lensing candidates. The confirmed true positives, obtained through visual inspection, are subsequently incorporated into the training set for iterative retraining of the model. Our pipeline successfully identified 485 cluster-scale strong lensing candidates, where 247 of them are newly found compared to other work in DESI data.

This article is organized as follows: In Section 2, we introduce the data we used, namely the galaxy cluster catalog from Zou et al. (2021), and then describe our mock program used to produce mock lensing images to generate our training set and validation set. Section 3 provides the construction of our neural network model and the training process, then in Section 4 we present the strong lensing candidates we found. Finally in Section 5, we discuss our findings and draw a conclusion. Throughout this paper, all RGB color composite images are generated using the g , r , and z band images from the DESI Legacy Imaging Surveys, which are assigned to the blue, green, and red color channels, respectively.

2. DATA

In this section, we first describe the 540,432 galaxy clusters identified in the DESI Legacy Imaging Surveys, as reported by Zou et al. (2021), in Subsection 2.1. These clusters may serve as input for our CNN-based methodology to

identify strong gravitational lenses. Next, we provide details on the mock framework developed to generate simulated lens images for training in Subsection 2.2, along with the preprocessing steps applied to the data in Subsection 2.3.

2.1. Observation data

The DESI Legacy Imaging Surveys (DESI-LIS) integrate three optical surveys to support spectroscopic target selection for the Dark Energy Spectroscopic Instrument (DESI): BASS (the Beijing-Arizona Sky Survey, [Zou et al. 2017](#)), DECaLS (the Dark Energy Camera Legacy Survey, [Blum et al. 2016](#)) and MzLS (the Mayall z -band legacy survey, [Silva et al. 2016](#)) three surveys, which covered a sky area of $\sim 14,000 \text{ deg}^2$ in the g, r , and z bands, and also integrated the latest WISE observations in the W1 and W2 bands ([Lang et al. 2016](#); [Meisner et al. 2019](#)). The cluster catalog used in this work is based on the latest data released (DR8) from DESI legacy imaging surveys at the time [Zou et al. \(2021\)](#) was published, which covered an area of approximately $20,000 \text{ deg}^2$. Details regarding the galaxy cluster images used in this study can be found in [Zou et al. \(2021\)](#).

These clusters were identified based on the photometric redshifts derived from DESI galaxies. As discussed in the work of [Zou et al. \(2019\)](#), they used the five-band deep photometry of the DESI legacy imaging surveys to obtain a catalog of accurate photometric redshifts and stellar masses for classified galaxies. They also applied some quality cuts to eliminate galaxies with very large photo- z uncertainty or very low luminosity. Based on the redshift catalog, [Zou et al. \(2021\)](#) applied the CFSFDP approach ([Rodriguez & Laio 2014](#)) similar to [Gao et al. \(2020\)](#) to detect clusters. A total of 540,432 galaxy clusters at $z \lesssim 1$ were finally identified. See Figure 8 for the number density of these clusters. The quality of this catalog is high enough to support our subsequent work. Monte Carlo simulation was performed to evaluate their detection approach and estimate the false detection rate, which showed that the false detection rate is about 3.1%, and the false rate can reach up to about 8%. The mass and richness of these clusters were also estimated by X-ray and radio observations, which were approximately $1.23 \times 10^{14} M_\odot$ and 22.5 respectively.

2.2. Mock data

The limited number (< 1000) of confirmed galaxy cluster-scale strong gravitational lenses presents significant challenges for training robust machine learning detectors. Recent galaxy-scale lens catalogs include more than 3,000 candidates ([Storfer et al. 2024](#)), the expected number of cluster-scale lenses remains approximately 1 order of magnitude lower due to the sparse spatial density of massive halos.

To address this limitation, a widely used approach is to generate mock lensing images. We develop a physically motivated simulation framework to produce mock cluster-scale lenses, incorporating several key components: (1) mass profiles constrained by observational data, derived from DESI photometric redshifts and luminosity-mass scaling relations; (2) simulated source galaxy populations based on [Collett \(2015\)](#); (3) wavelength-dependent PSF convolution using DECam instrument profiles; and (4) noise injection calibrated to DESI-LIS depth maps. Specifically, we construct the lensing potential, place a background source from the source catalog, and simulate the resulting arc. After applying PSF convolution and injecting noise, the arc is incorporated into the image.

To enhance realism and expand the parameter space, we also introduce adjustments to the mock lenses, ensuring that they better capture the diversity of cluster-scale lensing systems. This approach significantly improves the utility of our simulations for training machine learning models.

The methodology of our mock program is outlined as follows:

1. Parameter Extraction: We begin by selecting non-lensing clusters from the catalog by [Zou et al. \(2021\)](#), obtaining key parameters such as the RA and DEC of the Brightest Central Galaxy (BCG), the mass M_{500} , and the characteristic radius R_{500} for each galaxy cluster. Here, the subscript 500 indicates that the average density within R_{500} is 500 times the critical density of the universe, while M_{500} represents the total mass of the galaxy cluster contained within R_{500} . Then we extract photometric redshifts, axis ratios, position angles, ellipticities, and stellar mass estimates for each member galaxy from the galaxy cluster member catalog compiled by [Zou et al. \(2021\)](#).
2. Modeling the Lensing Potential: We model all member galaxies within the clusters as Singular-Isothermal-Ellipsoids (SIEs) using the parameters obtained in Step 1. The velocity dispersions are estimated following the method described in Eq. (2) of [Yue et al. \(2022\)](#). The lensing potential of the galaxy cluster is calculated based on its mass and radius using an elliptical Navarro-Frenk-White (eNFW) profile ([Navarro et al. 1996](#); [Golse & Kneib 2002](#)). The total lensing potential is determined by combining by summing the NFW potential of the

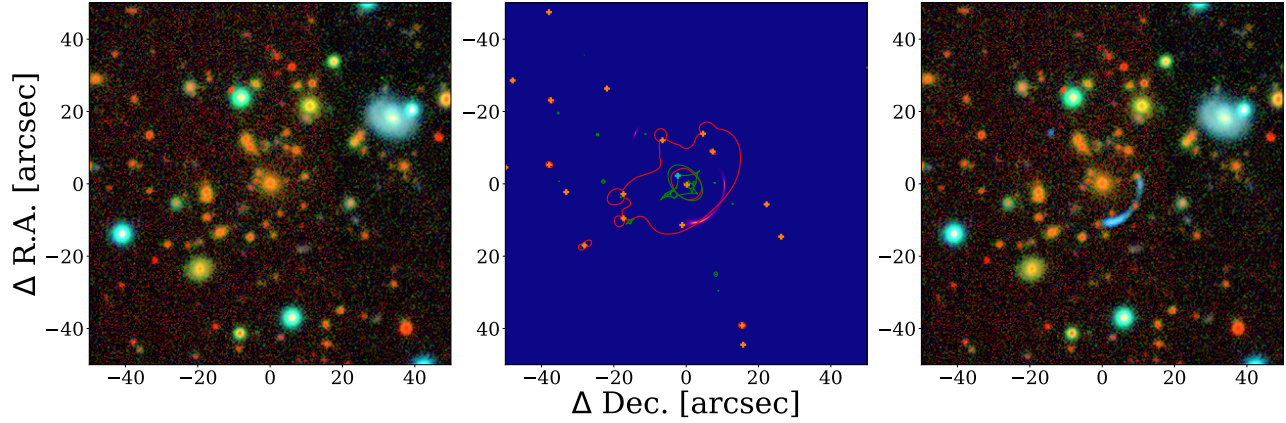


Figure 1. One example for our mock program, with side length of $100''$. Left: One selected non-lensed cluster image. Middle: The mock arc image to be added to the cluster image, together with the critical curves (red curve) and the caustics (green curve). The orange crosses indicate the positions of the member galaxies within the galaxy cluster, while the cyan cross indicate the source position. Right: The final mock lensing images.

cluster and the SIE potentials of the member galaxies. This combined potential allows us to compute key lensing properties, including deflection angles, magnification maps, critical curves, and caustics. Since the redshifts of the member galaxies are approximately the same, it is reasonable to approximate the total potential by directly summing the contributions from the cluster and its member galaxies.

3. We adopt a Sérsic profile for the source, with source parameters drawn from the catalog developed by [Collett \(2015\)](#), which provides a population of statistically realistic galaxy-galaxy strong lenses simulated for the Dark Energy Survey (DES) along with their observed properties. From this catalog, we extract key parameters of the sources, including their effective radii (r_e), magnitudes in three bands (g, r, z) and axis ratios (q). Note that we do not adopt the Sérsic index of the source galaxies in [Collett \(2015\)](#)'s catalog, since those values are all set to be unity. In practice, this assumption yields overly long arcs and fails to reproduce multiple images, and it also differs from the Sérsic indices of high-redshift galaxies in the simulation. Instead, we use the Sérsic index distribution of galaxies with redshifts of 1-2 in the simulation ([Xu et al. 2019](#)) as the Sérsic index distribution of our source galaxies. After defining the source properties, we place the centers of the mock sources in regions with high magnifications to generate lensed images.
4. Selection criteria for realistic arcs: We apply a selection criterion based on the size and color of the arcs to ensure that our training set spans a broad parameter space. Galaxy clusters with Einstein radius smaller than $5''$ are excluded from the final sample. The galaxies in the source catalog are predominantly high-redshift blue galaxies. However, during preliminary investigations, we identified several strong lensing systems with red arcs, which are underrepresented in the original catalog. To address this, we define three color categories based on the $g-r$ color index: red ($r+1.3 \leq g$), green ($r+0.8 \leq g \leq r+1.3$), and blue ($g \leq r+0.8$). The ratio of sources in these categories is set to 1:1:2, respectively, to better reflect the diversity of colors observed in real lensing systems.
5. Incorporating Point-Spread function (PSF) and noise: We convolve with a Gaussian PSF and then add Poisson noise. The PSF parameters are consistent with those of real PSF in the DESI Legacy Imaging Survey. Finally, we overlay the resulting arcs onto the original cluster images to obtain the final mock lenses.

Figure 1 shows an example of our mock image, and Table 1 gives the range and distribution of the parameters in our simulation. To assess the similarity between our mock images and real observations, we perform an unsupervised clustering analysis using the Uniform Manifold Approximation and Projection (UMAP; [McInnes et al. 2020](#)) algorithm, which is applied to feature representations extracted from both our mock lenses and the high-quality candidates of cluster-scale strong lenses given by the COOL-LAMPS project (see also subsection 4.2; [Mork et al. 2025](#)). The resulting UMAP visualization in Figure 3 shows that the mock lenses and the COOL-LAMPS lenses occupy overlapping regions in the reduced-dimensional feature space, suggesting that our mock images do not exhibit significant systematic

Table 1. Range and distribution of parameters used to generate the mock lensed images. Distributions for parameters in this table without analytic forms are shown in Figure 2.

Parameter	Range	Distribution
lens (eNFW)		
$\log_{10}(M_{500}/M_{\odot})$	$12.58 \sim 15.13$	-
Photometric redshift (BCG)	$0.01 \sim 1.04$	-
Position angle	$-90^{\circ} \sim -90^{\circ}$	uniform
Axis ratio	$0.4 \sim 1.0$	$\text{normal}(\mu = 0.75, \sigma = 0.1)$
lens (SIE members)		
$\log_{10}(M_{*}/M_{\odot})$	$8.04 \sim 12.69$	-
source (Sérsic)		
<i>g</i> -band magnitude	$21.3 \sim 29.5$	-
<i>r</i> -band magnitude	$21.0 \sim 28.0$	-
<i>z</i> -band magnitude	$20.3 \sim 28.3$	-
Effective radius	$0.00'' \sim 1.68''$	-
axis ratio	$0.2 \sim 1.0$	-
Redshift	$0.034 \sim 1.495$	-
Sérsic index	$0.4 \sim 4.0$	-

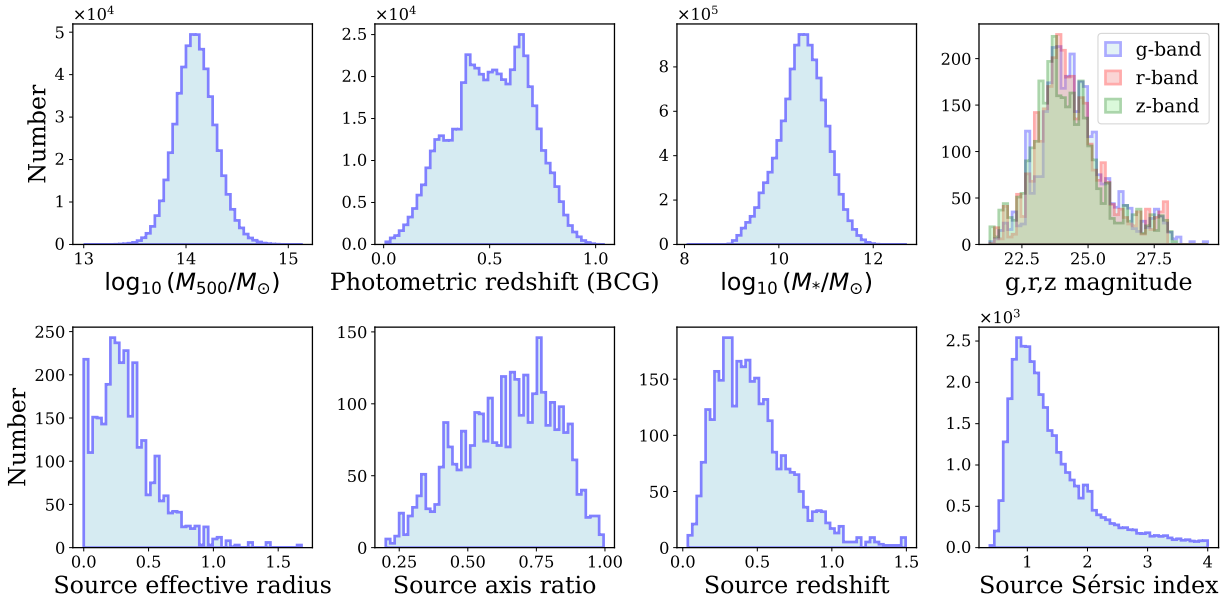


Figure 2. Distributions for parameters without analytic forms in Table 1. The source effective radius is units of arcseconds.

differences from the COOL-LAMPS lenses in the feature space captured by the UMAP algorithm, thus supporting the fidelity and applicability of the mocks for training strong lens classifiers based on CNNs.

2.3. Data preprocessing

Using our framework, we first select a sufficient number of non-lensed cluster images. These images are obtained in the photometric bands *g*, *r*, and *z*, with a default pixel size of $0.27''$ and dimensions of 371×371 pixels, corresponding to an approximate angular size of $100''$. Larger images are downloaded to accommodate potential subsequent tasks, such as cropping, thereby enhancing the flexibility of our analysis. Half of these images are used to generate mock lenses and are treated as positive samples (P), while the remaining half are left unprocessed and treated as negative samples (N).

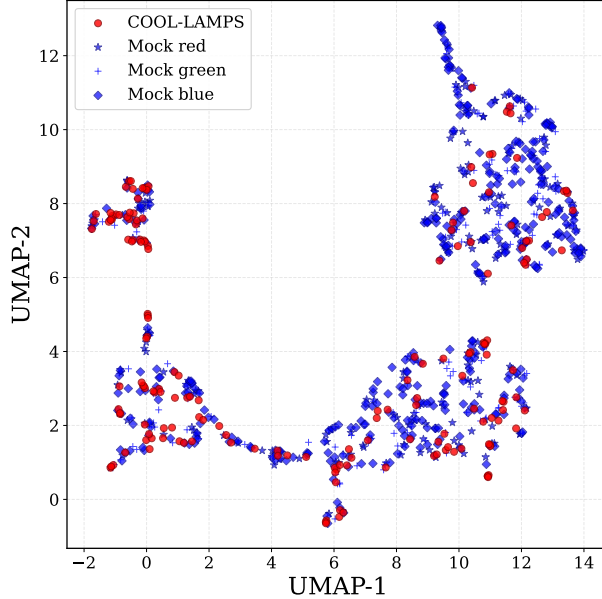


Figure 3. UMAP projection of randomly selected 800 mock lenses from the training set, including the systems with red (blue star), green (blue cross), and blue (blue diamond) sources defined in our manuscript (See Section 2.2). Red dots present the UMAP of 177 cluster-scale strong lenses from the COOL-LAMPS project (Mork et al. 2025).

To compose the training and validation sets, all images are cropped to a side length of 223 pixels ($60'' \times 60''$). The smaller image size allows CNN to better capture the spatial structure of the lens. The final training set and validation set consist of 100,000 images (50,000 P + 50,000 N) and 10,000 images (5,000 P + 5,000 N), respectively.

3. METHODOLOGY

In this section, we present the methodology of our work. First, we describe the convolutional neural network (CNN) employed and the associated training configuration. Next, we outline the methods employed to evaluate network training. Finally, we describe the iterative process adopted to enhance the results.

Our lens detection system utilizes a modified 18-layer Residual Neural Network (ResNet-18) architecture (He et al. 2015), reimplemented in PyTorch 1.10 with specific adaptations for processing astronomical images. This adaptation follows a similar approach to that used in Li et al. (2021), which has demonstrated efficient performance in comparable applications. The baseline model is reconfigured to accept 3-channel 223×223 pixel inputs, which correspond to the dimensions of our pre-processed galaxy cluster cut-outs that combine g , r , and z -band observations through chromatic stacking. The architecture consists of five residual block groups that progressively reduce spatial dimensions from 112×112 , following the initial convolution and max-pooling, to 7×7 feature maps. Strided convolutions with a stride of 2 are applied at strategic layers to preserve morphological features critical for lens identification. Each residual block contains two 3×3 convolutional layers with Batch Normalization (Ioffe & Szegedy 2015) and ReLU activation (Nair & Hinton 2010), maintaining gradient flow through identity shortcut connections. The network concludes with global average pooling, followed by a 2-dimensional fully connected layer that outputs logits optimized for binary classification between lensing systems and astrophysical false positives.

The network is trained using stochastic gradient descent with the Adam optimizer (Kingma & Ba 2017), configured with a batch size of 32, a learning rate of $\eta = 3 \times 10^{-6}$, and a weight decay of $\lambda = 10^{-1}$. The cross-entropy loss function (Goodfellow et al. 2016) is minimized:

$$-\sum_{i=1}^N y_i \log \hat{y}_i + (1 - y_i) \log(1 - \hat{y}_i), \quad (1)$$

where $y_i \in \{0, 1\}$ is label for the i th image (1 for lens and 0 for non-lens), and $\hat{y}_i \in [0, 1]$ is the probability predicted by the network. Training is performed on a Nvidia L40S GPU and required 4 hours to complete 200 epochs.

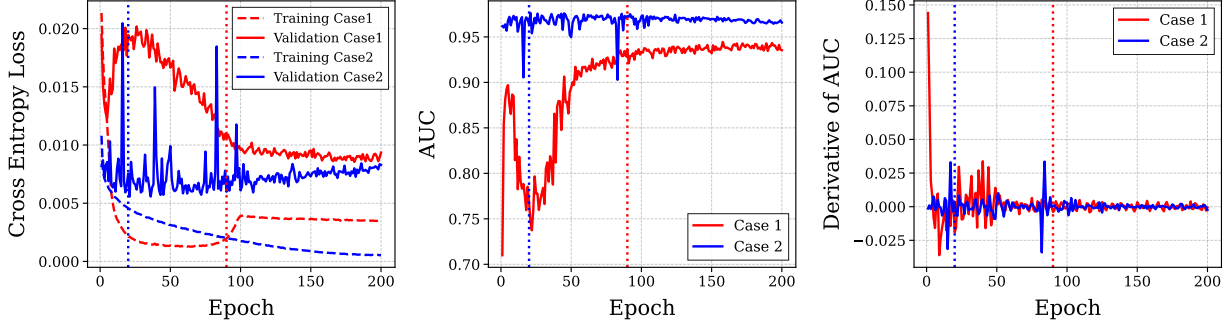


Figure 4. Left: The cross-entropy loss on the training and validation sets over 200 training epochs with two cases in the final iteration of our training. In Case 1, we adopt Adam optimizer, configured with a batch size of 32, a learning rate of 3×10^{-6} , and a weight decay of 1×10^{-1} . Moreover, in Case 2, We use a initial learning rate of 1×10^{-4} , a final learning rate of 1×10^{-5} , a weight decay of 1×10^{-2} , with Cosine Annealing. The vertical dashed line at epoch 20 and 90 indicates the early stopping points we selected in the two cases, which is the highest point of the AUC (Case 2), or the highest AUC before the training loss become abnormal (Case 1). Middle: The Area Under the ROC curve as a function of epoch in the same training session. Right: The derivative of AUC as a function of epoch in the same training session.

We quantify the detection capability of our gravitational lens identification system using Receiver Operating Characteristic (ROC) analysis. The network assigns a lens probability score $\hat{p} \in [0, 1]$ to each input image, representing the confidence level of lens detection. By systematically varying the classification threshold τ across the full probabilistic range ($0 \leq \tau \leq 1$), samples are dynamically classified as positive ($p \geq \tau$) or negative ($p < \tau$), generating four classification categories: True Positives (TPs, correctly identified lenses), False Positives (FPs, non-lens objects misclassified as lenses), True Negatives (TNs, correctly rejected non-lenses) and False Negatives (FNs, undetected lens systems). The diagnostic metrics are mathematically defined as follows:

$$TPR = \frac{TP}{TP + FN}, \quad (2)$$

$$FPR = \frac{FP}{FP + TN}, \quad (3)$$

where the True Positive Rate (TPR) measures the completeness of lens recovery, and the False Positive Rate (FPR) quantifies contamination from spurious detections. The ROC curve plots TPR against FPR parametrically across all possible τ values, with the Area Under the Curve (AUC) serving as a threshold-independent performance metric.

Figure 4 illustrates the variation of the loss function and AUC with its derivative across training epochs. In addition to the set of hyper-parameter configurations mentioned earlier (Case 1), we also compared and used another set of hyper-parameters configuration (Case 2), which use an initial learning rate of 1×10^{-4} , a final learning rate of 1×10^{-5} , a weight decay of 1×10^{-2} , with Cosine Annealing. It shows that in Case 1, after overcoming an initial local optimum, the AUC increases rapidly to approximately 0.93–0.95 before entering a period of fluctuation. However, the training loss begins to increase abnormally after 100 epochs, rendering the model unreliable beyond this point. In Case 2, the validation loss initially reached a relatively low level, but then gradually increased due to overfitting. Although the AUC in Case 2 reached a value of approximately 0.97, which was higher than that in Case 1, the highly fluctuating loss curve suggests that the model may be unstable. Moreover, the excessively high AUC also poses the risk of overfitting on the mock images. Therefore, we selected a deep learning model with an AUC of 0.94 from those in Case 1. The ROC curve of the best model on the validation set from one of our training sessions is shown in Figure 5. On the simulated testing data, the model achieves an area under the curve (AUC) of 0.939.

We also define two additional metrics:

$$\text{Precision} = \frac{TP}{TP + FP}, \quad (4)$$

$$\text{Recall} = TPR = \frac{TP}{TP + FN}, \quad (5)$$

which are used to determine the probability threshold for human inspection. Figure 5 shows the Precision-Recall Curve (PRC) of the best model in one of our training sessions. In an ideal PRC, the curve would pass through

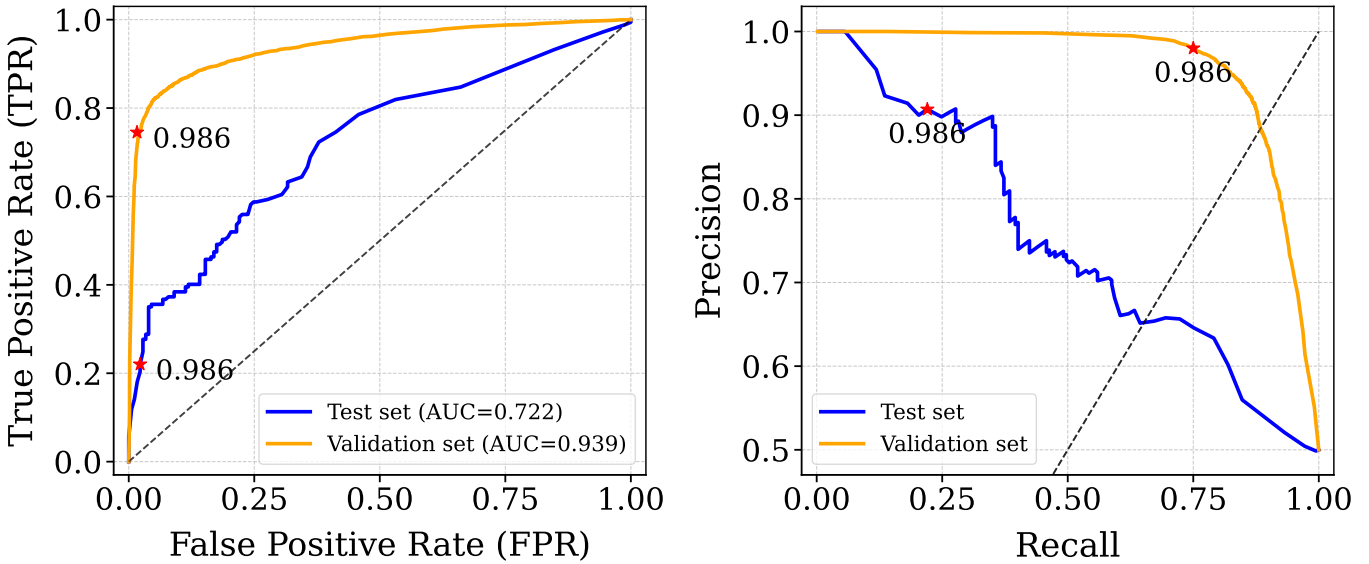


Figure 5. Comparison of the performance of our classifier evaluated with validation and testing sets separately. The left panel shows the ROC curve (orange line) of our classifier on the validation set containing our mock images with the area under the curve (AUC=0.939). And the ROC curve (blue line) of our classifier on the testing set containing the lens candidates from the COOL-LAMPS project (Mork et al. 2025) with the area under the curve (AUC=0.722). The right panel shows the PR curve for the above two cases. We also mark the threshold (0.986) adopted in last iteration with red stars.

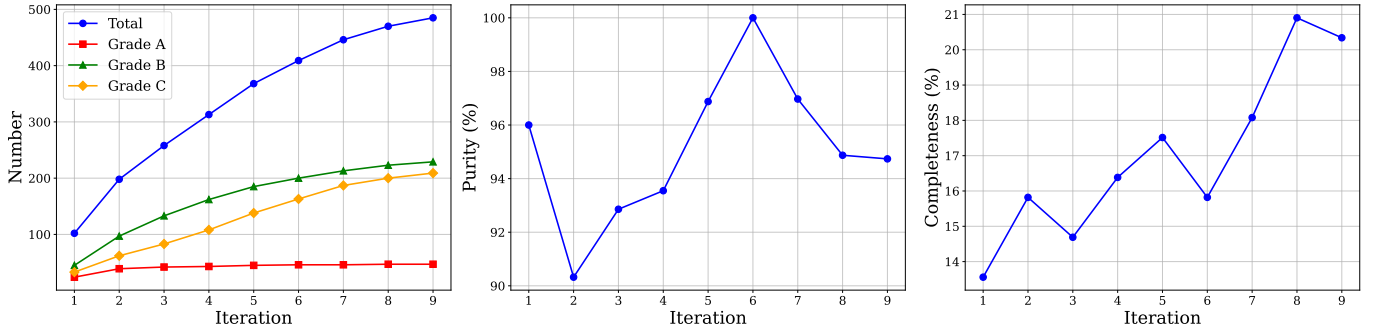


Figure 6. Performance of our classifier along with the iterations. Left Panel shows the cumulative number at each iteration, shown for all candidates and separately for the three grades. The middle and right panels shows the Purity and completeness when applying our classifier to the testing set containing the lens candidates from the COOL-LAMPS project.

the point (1, 1), where all thresholds would converge. The PRC is consulted to select the probability threshold for inspection, balancing precision (purity) and recall (completeness). For this work, we prioritized a high-precision point to demonstrate the model’s accuracy and minimize the number of false positives, resulting 4,000 positive images.

To improve completeness while maintaining a low false-positive rate, we adopt an iterative search procedure for strong-lensing candidates. In the initial iteration, we manually filter the top 4,000 samples with the highest scores given by the classifier trained by the mock images described in Section 2.2, and the corresponding threshold of the score is 0.99048. We then identified 102 true-positive candidates. After that, we removed them from the data pool for mining lens candidates and incorporated them into the positive sample of the training set for the subsequent training-filtering-updating loops. The details of the performance and outcomes of the classifier in each iteration are shown in Table 2.

Figure 6 shows the number of our candidates with grade A~C (see Section 4.1). We repeat this iterative process until the number of detected strong-lensing candidates no longer shows significant improvement. Based on our experience, nine iterations are typically sufficient to achieve satisfactory results, since the quantity of the highest-quality grade A

samples did not increase significantly in the final several iterations. This systematic refinement enriches the training data and enhances the model's robustness in identifying strong gravitational lenses.

Table 2. Statistics of candidates discovered during iterations (Iter.), including our threshold to select the top 4000 samples (Thresh.); the lowest score for our newly discovered candidates (Thresh.TP); the number of our newly discovered candidates (New) and cumulative candidates (Cum.), and the cumulative candidates with Grade A to Grade C; the purity (Purity) and completeness (Compl.) on the testing set made by COOL-LAMPS strong lensing (Mork et al. 2025).

Iter.	Thresh.	Thresh.TP	New	Cum.	Cum. A	Cum. B	Cum. C	Purity (%)	Compl. (%)
1	0.99048	0.99062	102	102	24	45	33	96.0	13.6
2	0.96557	0.96641	96	198	39	97	62	90.3	15.8
3	0.97076	0.97081	60	258	42	133	83	92.9	14.7
4	0.96627	0.96647	55	313	43	162	108	93.5	16.4
5	0.97106	0.97146	55	368	45	185	138	96.9	17.5
6	0.99082	0.99116	41	409	46	200	163	100.0	15.8
7	0.97178	0.97300	37	446	46	213	187	97.0	18.1
8	0.96549	0.96645	24	470	47	223	200	94.9	20.9
9	0.98628	0.98748	15	485	47	229	209	94.7	20.3

4. RESULTS

In this section, we present our results. Subsection 4.1 introduces the grading system for the identified candidates and the distribution of their parameters. Subsection 4.2 compares our findings with those of previous studies, and subsection 4.3 highlights specific examples that demonstrate the effectiveness of our scoring system. Finally, subsection 4.4 gives some other discussion.

4.1. Inference and Lens Candidates

Our analysis of 540,432 galaxy clusters from the Zou et al. (2021) catalog identify a total of 485 strong gravitational lensing candidates using our trained classification model. These candidates are graded based on the prominence of their gravitational lensing features and galaxy cluster characteristics. The grading system is as follows:

- 1. Characteristics of galaxy clusters:** A system is considered to satisfy the requirements if the number of member galaxies in the field of view exceeds 10. Otherwise, it is regarded as lacking the distinct characteristics of a galaxy cluster.
- 2. Arc prominence:** The system must include a lensed arc that is clearly observable, with high relative brightness, a significant length-to-width ratio, and a high degree of circumferential completeness. Arcs that fail to meet all these criteria are considered non-prominent.

The scoring rules are defined as follows:

- If Criterion 1 is satisfied:
 - and if Criterion 2 is also satisfied, the score is **A**.
 - and if Criterion 2 is not satisfied but an arc is visual, the score is **B**.
 - and if Criterion 2 is not satisfied and the arc is nearly invisible, the score is **C**.
- If Criterion 1 is not satisfied:
 - and if Criterion 2 is satisfied, the score is **B**.
 - and if Criterion 2 is not satisfied, the score is **C**.

After all seven authors have completed their respective grading, we canceling out A and C grades against each other. With seven scoring experts, the remaining number of grades is always odd and consists only of A and B or B and C. In this case, the majority grade is selected as the final grade (for example, 4A, 2B, 1C; after cancellation, it becomes 3A, 2B, and A is chosen). We finally identify 47 Grade A candidates (9.7%), 229 Grade B candidates (47.2%), and 209 Grade C (43.1%) candidates. Examples of candidates from each grade are shown in Figure 7, while the positions of all candidates in the sky are displayed in Figure 8.

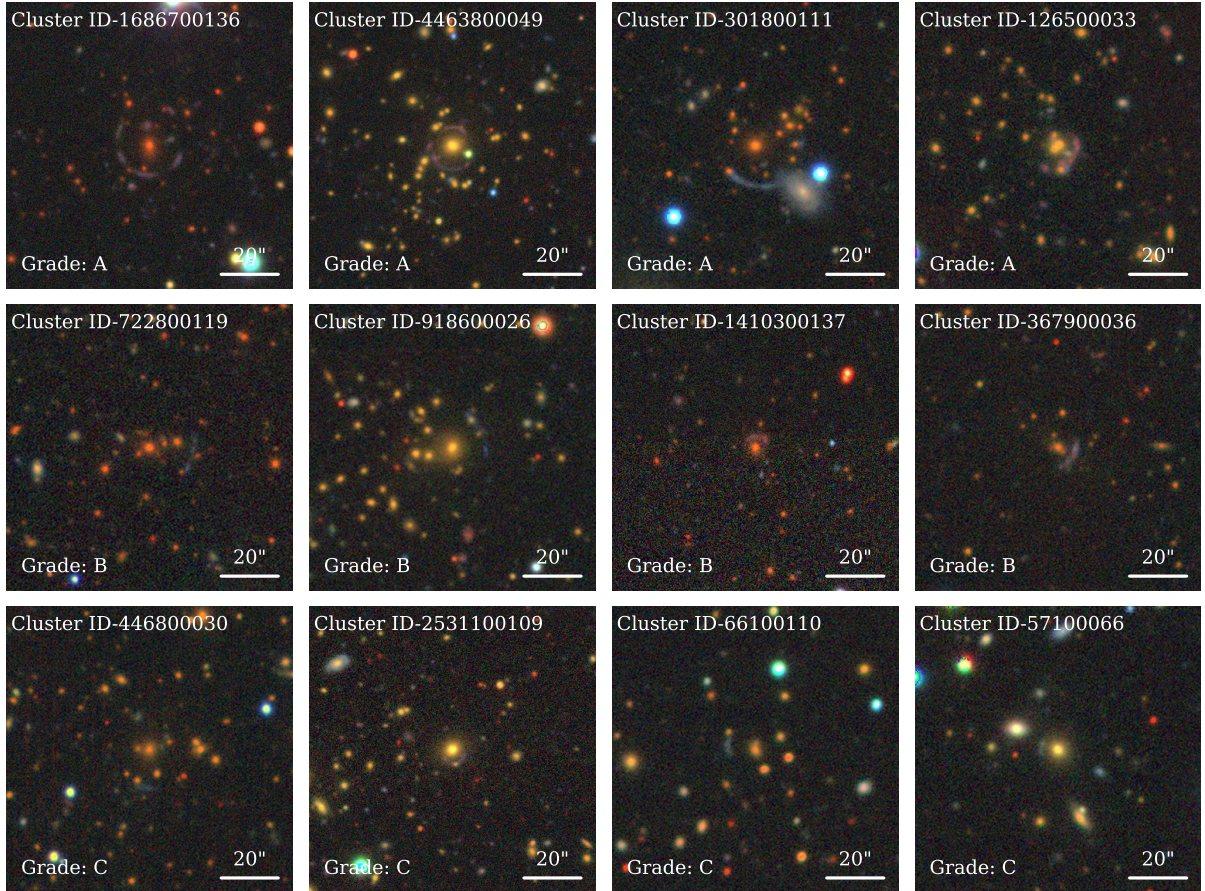


Figure 7. Selected twelve typical strong lensing candidates with Grade A, B and C. Grade A systems exhibit prominent, long, and bright arc-like images, with distinct features of background galaxy clusters. In contrast, the arcs in Grade B and Grade C systems are fainter. For all images, north is up, and east to the left. The top left corner of each image is the galaxy cluster ID of each image in Zou et al. 2021; the grade is indicated at the bottom left corner.

Our systematic analysis of lens candidate properties reveals key demographic trends (Figure 9). The cluster masses M_{500} , derived from Zou et al. (2021) catalog through X-ray and radio observations, exhibit a distribution range of $10^{13.67 \sim 14.97} M_{\odot}$, which is consistent with our training samples. However, the peak mass of our candidates ($\sim 10^{14.6} M_{\odot}$) is higher than that of the training set ($\sim 10^{14.2} M_{\odot}$). The figure also illustrates the distribution of the BCG photometric redshift and effective radius of our candidates, which align closely with the distribution in our training samples. Notably, the Einstein ring radius distribution differs. While the training set includes only samples with Einstein radii greater than $5''$ our candidates include some with smaller Einstein rings. It is important to note that the Einstein ring radii here are measured approximately as the distance from the arc to the lens center, which differs from the definition used in the training set. Furthermore, although our model is designed to identify strong lensing with prominent arcs at galaxy cluster scales, it is expected to detect some by-products at galaxy or group scales. In Figure 10, we show a corner plot for the correlations among these four parameters, and also labeled the grade of these candidates assigned by authors, showing that candidates with Grade A have higher M_{500} than others.

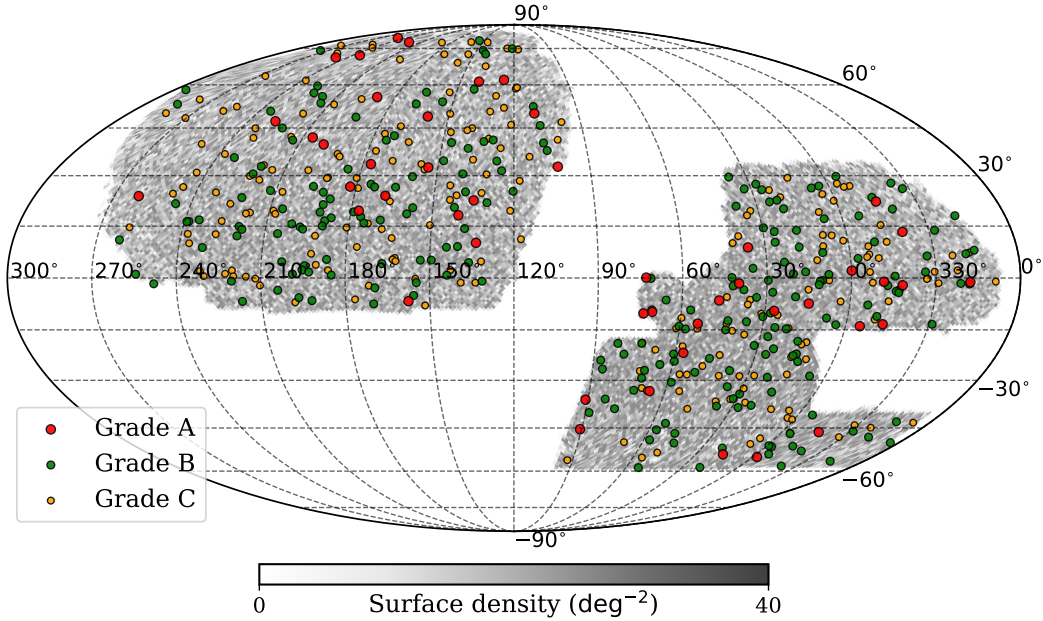


Figure 8. The 485 candidates over the surface density map of clusters in the catalog from Zou et al. 2021.

4.2. Comparison with other strong lensing catalogs

We compared our results with other studies that identified strong lensing candidates in DESI data. The first comparison is with a series of paper by Huang et al. (2020), Huang et al. (2021), and Storfer et al. (2024), which utilized deep residual neural network to search for strong lensing in DESI Legacy Imaging Surveys DR8 and DR9. The second comparison is with the project Chicago Optically selected Lenses Located at the Margins of Public Surveys (COOL-LAMPS; Mork et al. 2025), which relied on a large team of researchers to manually perform visual searches for strong gravitational lenses in DESI data.

In the recent work by Storfer et al. (2024) of the first series work, they found a total of 3,057 strong lens candidates with Grades A, B and C, and also Grade D candidates which they did not count in their paper but included in their project website. From their catalog, we recover 227 previously known systems and identify 258 new candidates. These new detections include 20 candidates of Grade A (7.8%), 96 candidates of Grade B (37.2%) and 142 candidates of Grade C (55.0%).

Figure 11 demonstrates that our candidates exhibit a higher number density at low photometric redshifts. This discrepancy could be attributed to the smaller Einstein ring radii typically associated with low-redshift galaxy-scale lenses, which are more challenging to detect. In contrast, our CNN architecture, optimized specifically for cluster-scale lenses with higher Einstein radii, is less affected by this limitation. An analysis of some candidates from Storfer et al. (2024) reveals masses within the Einstein radius of approximately $\sim 2 \times 10^{12} M_{\odot}$, characteristic of galaxy-scale systems. This highlights our method's enhanced sensitivity to identifying lensing systems at the galaxy cluster scale.

For the overlapping candidates, we assigned 27 to Grade A (11.9%), 133 to Grade B (58.6%) and 67 to Grade C (29.5%), while Storfer et al. (2024) gave 106 Grade A (46.7%), 47 Grade B (20.7%), 52 Grade C (22.9%) and 22 Grade D (9.7%). Our grading strategy not only accounts for the strength of the gravitational lensing signal but also considers the significance of the galaxy cluster characteristics. As a result, our grades are generally lower than those given by Storfer et al. (2024). However, there are exceptional cases where our grades are higher. We will briefly discuss these cases later in Section 4.3.

We also compare our findings with another project called COOL-LAMPS finding cluster-scale strong gravitational lenses. In their recent paper (Mork et al. 2025), they report a total of 177 cluster-scale strong gravitational lens systems, and all of these systems are included in Zou et al. (2021). Of our 485 systems, 429 are newly identified by our work, comprising 32 Grade A (7.5%), 193 Grade B (45.0%) and 204 Grade C (47.5%). For the overlapping candidates, we have 15 Grade A (26.8%), 36 Grade B (64.3%) and 5 Grade C (8.9%), indicating that our machine learning based

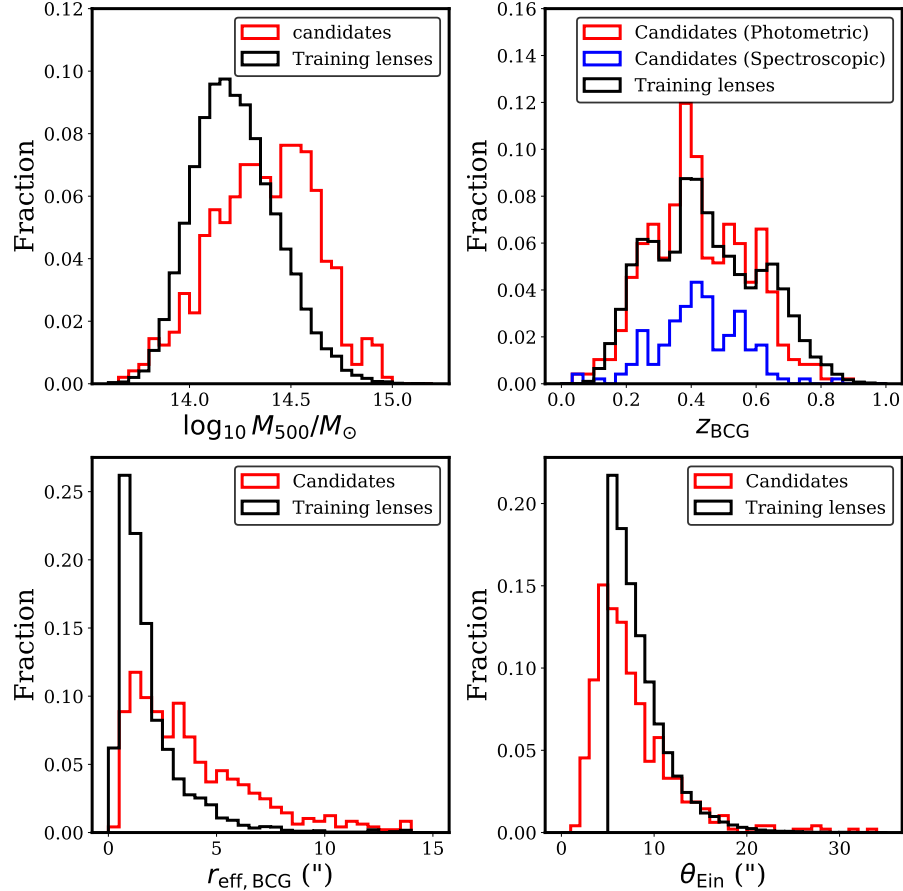


Figure 9. Parameters distribution of our strong lensing candidates and training samples. Upper left: The M_{500} of the cluster. Upper right: The redshift of BCGs, including the photometric redshifts of all candidates (red), as well as the subset of candidates whose spectroscopic redshifts can be found in DESI DR1 (Collaboration et al. 2025, in purple). Lower left: The effective radius of BCG. Lower right: The Einstein radius, which is approximately estimated by taking the average of the distances from the BCG to several points on the arcs.

method can complement the manual searches. We also examined 122 COOL-LAMPS candidates that our method failed to detect. The vast majority of these images would receive a low grade according to our grading strategy. Only fewer than 6 samples (Figure 12) could receive a Grade A, demonstrating that our method has good completeness in identifying candidates at the Grade A level.

Based on the matching of the two projects, there are a total of 247 candidates among our candidates who are not discovered by them. Among them, 16 are Grade A (6.5%), 90 are Grade B (36.4%), and 141 are Grade C (57.1%).

4.3. Grading strategy

We present a few examples with our grading strategy whose grades show significant variation among the authors. In Figure 13 we highlight the eight candidates with the largest standard deviations. The galaxy cluster 2365300017 (first row, first column) has a ring-galaxy like BCG, which also looks like an Einstein ring. The color of the ring appears quite similar to that of BCG, and such a perfect Einstein ring is very rare among strong-lensing systems. We believe the final Grade C, assigned based on our third grading strategy, is more reliable than the Grade B given by the other two strategies (see Section 4.1). For the other seven images, the arcs are noticeably different in color from the member galaxies, making them appear observable. This led some of the authors to give Grade A. However, compared to other strong lensing candidates, these arcs are relatively short and faint. As a result, all of them were ultimately assigned Grade B as a compromise.

In Section 4.2, we note several cases where the grades in this work are higher than those in Storfer et al. (2024), which is unusual. For instance, the galaxy cluster 249880056, also labeled Abell 370 in Abell (1958), features a giant

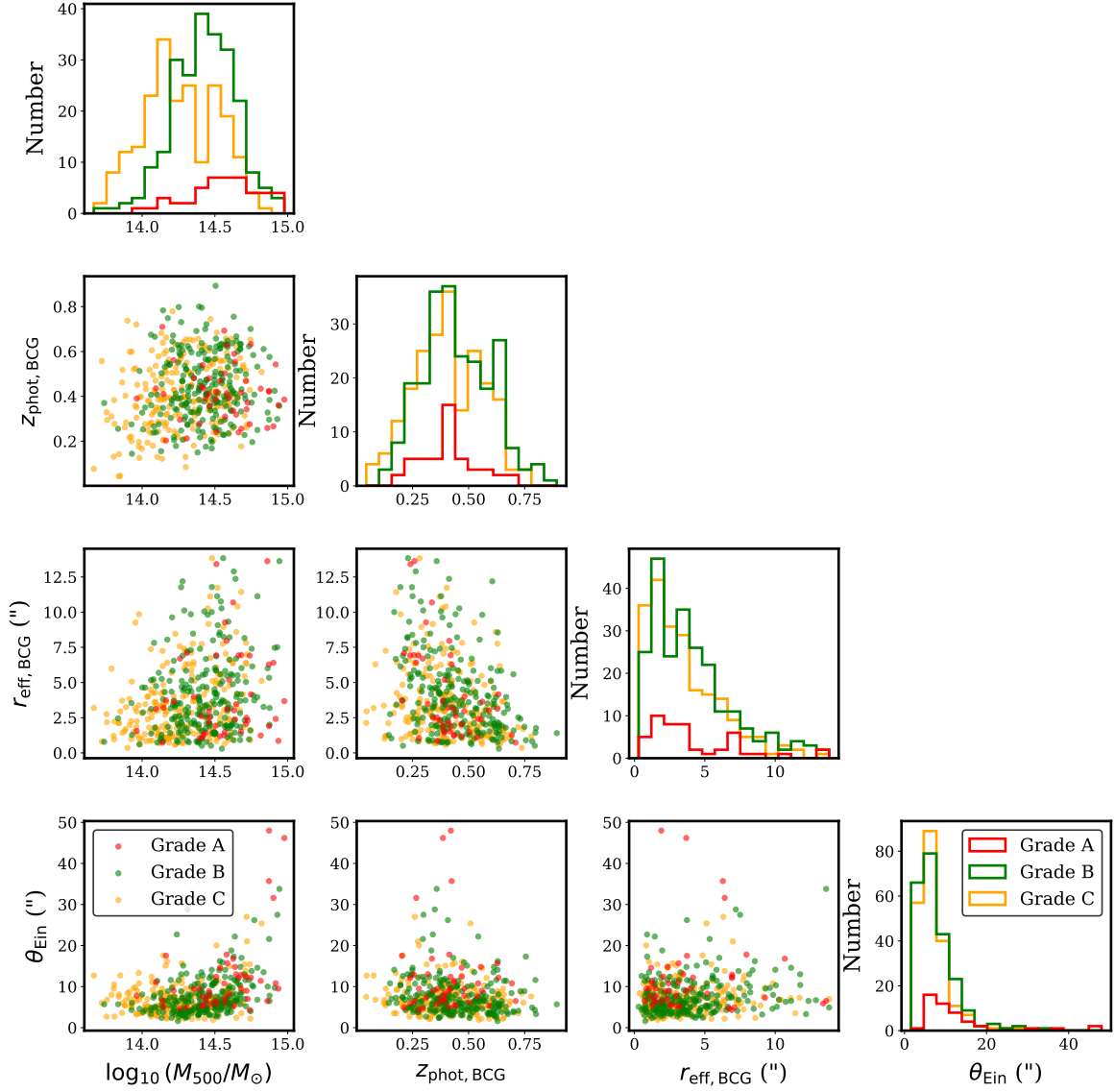


Figure 10. Corner plots illustrate the distributions and correlations among four key parameters for three graded strong lensing candidates displaying scatter plots with Grade A (red), Grade B (green), and Grade C (orange) clusters. The diagonal presents the parameter distributions. The four parameters are: (a) cluster mass M_{500} , (b) Photometric redshift of BCG, (c) Effective of BCG, and (d) Einstein Radius.

arc which is about $40''$ far from its BCG, and is Grade A in this work and Grade D in [Storfer et al. \(2024\)](#). In the training set and recognition work of our network, we have cropped the image side length to $60''$, which cannot catch that giant arc. However, the images used in our grading work are not cropped, allowing all authors assigned Grade A to this candidate. The image cutout size in [Storfer et al. \(2024\)](#) is even smaller than us ($26''$), which could not capture obvious strong lensing signal, and may be the reason why they gave a low grade. Machine learning methods can capture some gravitational lensing features that are difficult to identify visually. This might be the reason why it can identify these candidates even when the image dimensions are relatively small.

4.4. Other discussion

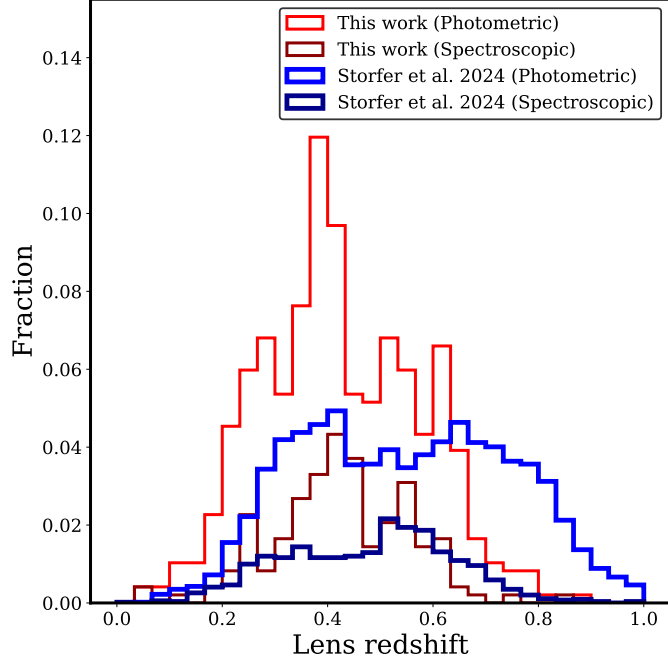


Figure 11. Lens redshift of candidates from our work and Storfer et al. 2024. For our work, we show the photometric redshift for all the candidates (red), as well as the subset of candidates whose spectroscopic redshift can be found in DESI DR1 (purple). For Storfer et al. 2024, we show either photometric (black line) or spectroscopic from SDSS Data Release 17 (blue line).

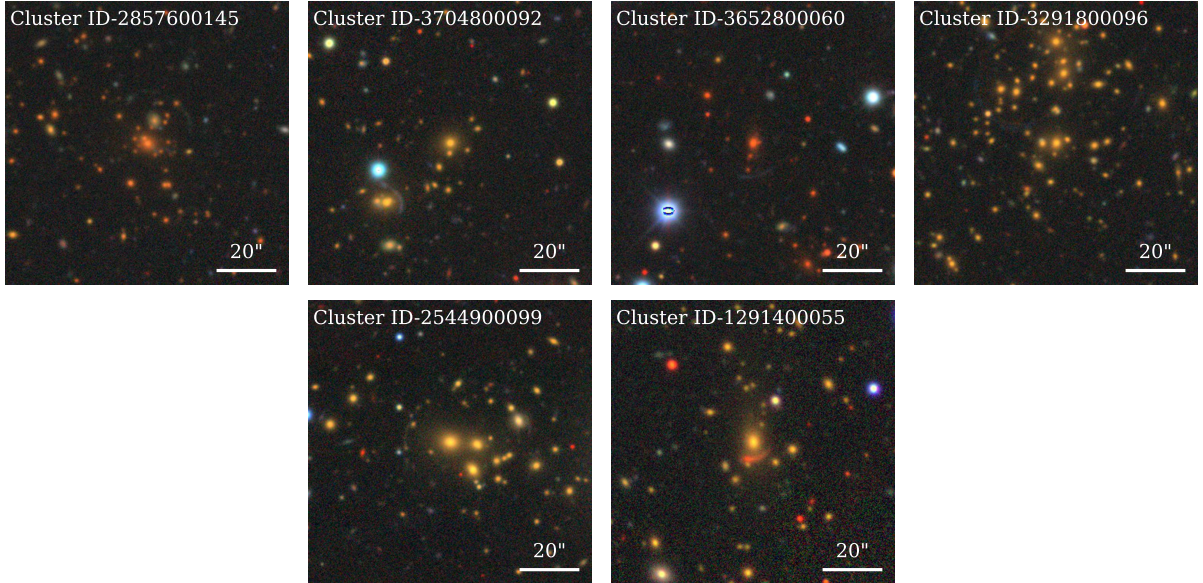


Figure 12. Six strong lensing systems identified in project COOL-LAMPS but were not find by this work. The arcs in this six images are generally fainter compared to our Grade A candidates, and the centers of the arcs in the upper-middle and lower-left images do not point towards the BCG of the cluster. Other systems with even low quality are not shown here.

In the process of searching, the vast majority of false positives consist of the images with similar features to the strong lensed arcs for which the specific cause of misclassification remains unclear, suggesting the deep learning model may be sensitive to subtle or complex morphological patterns. However, during the interactive procedure, we can identify and categorize a subset of significant false positives attributable to recognizable features, including the spiral arms of

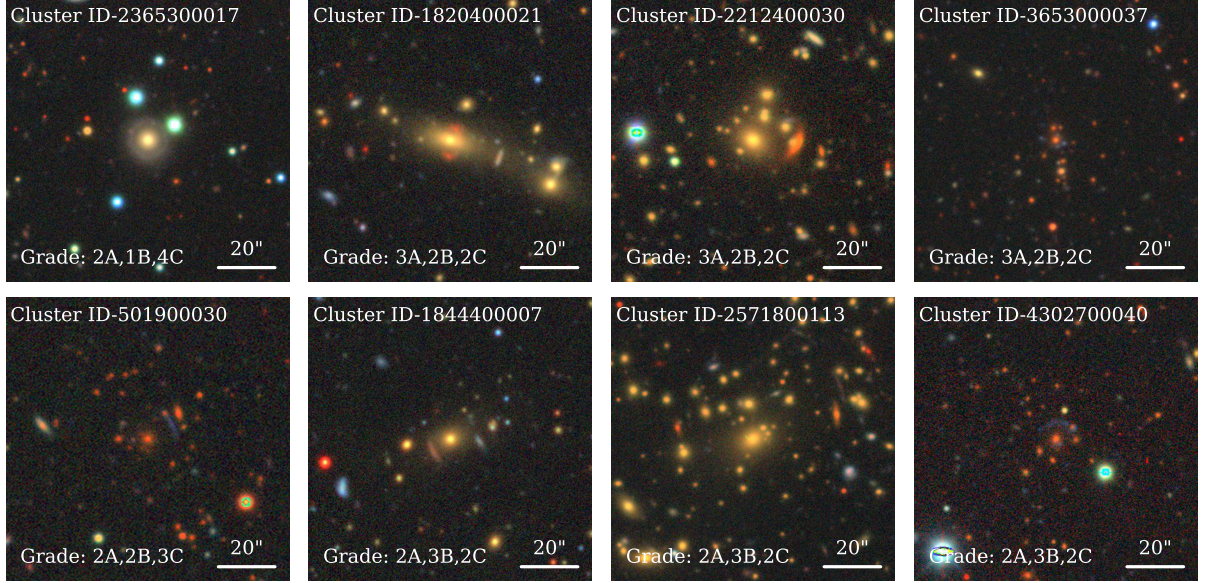


Figure 13. Eight strong lensing candidates with the largest standard deviation among the grades by 7 authors (we give A a score of 3, B of 2, and C of 1). For all images, north is up, and east to the left. The top left corner of each image is the galaxy cluster ID of each image in Zou et al. 2021; bottom left corner, the grades number by 7 authors.

late-type galaxies, edge-on disk galaxies, ringed galaxies, and stellar streams, all of which can produce arc-like features. Additionally, the background galaxies with significant photometric color contrast against the central brightest cluster galaxy (BCG) can occasionally generate false lensing signals of multiple lensed images, which can not be determined with images only but request further spectrum information.

It is worth noting that modern architectures such as EfficientNet (Tan & Le 2020), ConvNeXt (Liu et al. 2022), and Vision Transformers (Dosovitskiy et al. 2021) are not used in this work, since the core objective of this study is not to compare state-of-the-art networks, but to systematically examine whether human-in-the-loop collaboration can enhance detection performance even with a well-established baseline model. We selected a modified ResNet-18 for its stability, interpretability, and wide adoption in earlier lens-finding studies (Lanusse et al. 2018; Li et al. 2021; Petrillo et al. 2019), which provides a consistent and reproducible foundation for evaluating the added value of human expertise. While we fully acknowledge the strong potential of newer architectures (Parlange et al. 2025; Nagam et al. 2025; Yang et al. 2025) and agree they represent a promising future direction. Also, effectively integrating them with human-in-the-loop interaction requires careful design to ensure meaningful synergy between model capacity and human judgment. Nevertheless, we plan to explore its extension to more advanced architectures in subsequent research, where both model selection and human integration can be co-optimized.

5. SUMMARY

In this work, we present a systematic search for candidates of galaxy cluster-scale strong gravitational lensing systems based on the galaxy cluster catalog identified by Zou et al. (2021) from the DESI Legacy Imaging Surveys DR8, covering approximately $20,000 \text{ deg}^2$ of the extragalactic sky. We first designed a 3-step approach, including a strong lens simulator for creating positive samples in the initial training set, a binary classifier built upon Resnet-18 for identifying lens candidates, and human inspection to improve the purity of the outcomes further. Then, we interactively loop the classification and human inspection procedures to achieve stable completeness of the lens candidates. Subsequently, all the authors of this work visually assessed the candidates according to the features of strong lensing and galaxy clusters. As a result, we identified 485 high-confidence cluster lens candidates. The halo mass, $\log(M_{500}/M_{\odot})$, of these candidates ranges from $10^{13.67}$ to $10^{14.97} M_{\odot}$, and their brightest cluster galaxy (BCG) photometric redshift spans from 0.04 to 0.89.

The iteration starts with applying a binary classifier trained with the initial training sets (50,000 P + 50,000 N) to galaxy clusters from DESI Legacy Survey DR8. We chose a relatively conservative configuration of hyperparameters (a batch size of 32, a learning rate of 3×10^{-6} , and a weight decay of 1×10^{-1}). The training process continues until the

point where the Area Under the ROC Curve (AUC) reaches its maximum value, after which the model's loss begins to increase abnormally, approximately 0.94. Although the AUC of the model we selected was not as high as that of the more aggressive configuration (a batch size of 32, an adaptive learning rate with an initial value of 1×10^{-4} and final value of 1×10^{-5} , and a weight decay of 1×10^{-2} , with Cosine Annealing), leading to an AUC of 0.97, more robust evaluation beyond AUC is required to avoid the potential overfitting issue and find the optimal configuration of the hyperparameters for the entire process, which is one of our focuses in the future studies. After that, the first author visually selected candidates from the 4,000 samples with the highest scores given by the model, and added them to the original training set. The classifier is then retrained using this updated dataset. The loop will stop when the classification performance is stable (see Figure 6). We implement nine iterations in this study. At last, through visual inspection using a three-tier grading system based on arc morphology and Einstein radius scale (criteria detailed in Section 4) by all the authors of this paper, we classify 47 candidates as grade A (obvious arcs in cluster scale), 229 as grade B (probable arcs or galaxy scale), and 209 as grade C (possible arcs and galaxy scale).

In comparison to relevant studies, our strategy emphasizes the identification of cluster lens candidates in a Human-in-the-loop-like manner (Fu et al. 2024). First, relative to Storfer et al. (2024)'s CNN-based galaxy-scale lens search, our training set is optimized based on characteristics of cluster lenses (see Subsection 2.2), which is a key reason why we found hundreds of novel cluster lens candidates. Second, compared with the human-intensive method of COOL-LAMPS (Mork et al. 2025), our CNN-based approach achieves a computational efficiency of $< 10\text{ms}$ per image classification, demonstrating the viability of machine learning for large-area surveys. Furthermore, our strategy achieves a simple human-computer interaction by retraining the model through iterative processes, incorporating manually identified true positive samples into the training set. This approach balances the accuracy of manual search and the speed of machine learning methods. Cross-matching with existing catalogs reveals that 247 candidates (50.9% of the sample) show no counterparts in Storfer et al. (2024) or the COOL-LAMPS project (Mork et al. 2025), which include 16 new grade A systems and 90 grade B, 141 grade C.

However, several aspects of our approach require improvement. First, there are discrepancies between the distributions of the training sets and those of the candidates (see Figure 9), which suggests that we should incorporate more realistic parametric distributions when generating training sets to enhance the classification performance of the deep learning module. Second, the current ResNet-18 achieves an AUC of $\gtrsim 0.94$ in validation tests at each step, while advanced architectures like Vision Transformers (Dosovitskiy et al. 2021) have the potential to improve the AUC to 0.999 through better arc morphology capture. Thus, it is sensible to explore novel AI techniques in future investigations. Third, our manual verification process (about 2.5 hours per 1000 candidates) in the iterative process could be streamlined using active learning techniques, such as Bayesian active learning (Houlsby et al. 2011), to prioritize ambiguous cases, potentially cutting human effort by 50%.

To summarize, with a 3-step lens-finding approach, we discover 485 high-confidence cluster lens candidates in total cluster lens candidates from DESI Legacy Surveys DR8, and 247 of them are new. This dataset is valuable for examining mass assembly histories through joint strong and weak lensing analyses. Among the findings, 16 Grade A systems are suitable for putting strong constraints on the concentration-mass relation of dark matter halos and the cosmological parameters, such as the matter density, Ω_m . In addition, comparing observations taken at different epochs could be beneficial in detecting lensed transients. We encourage observers to explore the best candidates for these applications in the future.

ACKNOWLEDGEMENTS

Z.Z. acknowledges the High-performance Computing center at Westlake University and the Tsinghua Astrophysics High-Performance Computing platform for providing computational and data storage resources that have contributed to the research results reported in this work. N.L. acknowledges the support of the CAS Project for Young Scientists in Basic Research (No. YSBR-062), the Ministry of Science and Technology of China (No. 2020SKA0110100), and the support of the Association for Astronomy X A.I. (A^3), funded by the Science and Education Integration Funding of the University of Chinese Academy of Sciences. Z.H. acknowledges support from the National Natural Science Foundation of China (Grant No. 12403104). H.Z. acknowledges the supports from the National Key R&D Program of China (grant Nos. 2023YFA1607804 and 2022YFA1602902) and the National Natural Science Foundation of China (NSFC; grant Nos. 12120101003 and 12373010).

REFERENCES

Abell, G. O. 1958, *ApJS*, 3, 211, doi: [10.1086/190036](https://doi.org/10.1086/190036)

Alard, C. 2006, arXiv e-prints, astro, doi: [10.48550/arXiv.astro-ph/0606757](https://doi.org/10.48550/arXiv.astro-ph/0606757)

Blum, R. D., Burleigh, K., Dey, A., et al. 2016, in American Astronomical Society Meeting Abstracts, Vol. 228, American Astronomical Society Meeting Abstracts #228, 317.01

Caminha, G. B., Grillo, C., Rosati, P., et al. 2016, *A&A*, 587, A80, doi: [10.1051/0004-6361/201527670](https://doi.org/10.1051/0004-6361/201527670)

Coe, D., Umetsu, K., Zitrin, A., et al. 2012, *ApJ*, 757, 22, doi: [10.1088/0004-637X/757/1/22](https://doi.org/10.1088/0004-637X/757/1/22)

Coe, D., Zitrin, A., Carrasco, M., et al. 2013, *ApJ*, 762, 32, doi: [10.1088/0004-637X/762/1/32](https://doi.org/10.1088/0004-637X/762/1/32)

Coe, D., Salmon, B., Bradač, M., et al. 2019, *ApJ*, 884, 85, doi: [10.3847/1538-4357/ab412b](https://doi.org/10.3847/1538-4357/ab412b)

Collaboration, D., Abdul-Karim, M., Adame, A. G., et al. 2025, Data Release 1 of the Dark Energy Spectroscopic Instrument. <https://arxiv.org/abs/2503.14745>

Collett, T. E. 2015, *ApJ*, 811, 20, doi: [10.1088/0004-637X/811/1/20](https://doi.org/10.1088/0004-637X/811/1/20)

Dey, A., Schlegel, D. J., Lang, D., et al. 2019, *AJ*, 157, 168, doi: [10.3847/1538-3881/ab089d](https://doi.org/10.3847/1538-3881/ab089d)

Dosovitskiy, A., Beyer, L., Kolesnikov, A., et al. 2021, An Image is Worth 16x16 Words: Transformers for Image Recognition at Scale. <https://arxiv.org/abs/2010.11929>

Euclid Collaboration, Walmsley, M., Holloway, P., et al. 2025, arXiv e-prints, arXiv:2503.15324, doi: [10.48550/arXiv.2503.15324](https://doi.org/10.48550/arXiv.2503.15324)

Faure, C., Kneib, J.-P., Covone, G., et al. 2008, *ApJS*, 176, 19, doi: [10.1086/526426](https://doi.org/10.1086/526426)

Fu, M.-X., Song, Y., Lv, J.-M., et al. 2024, *Chinese Physics C*, 48, 095001, doi: [10.1088/1674-1137/ad50ab](https://doi.org/10.1088/1674-1137/ad50ab)

Gao, J., Zou, H., Zhou, X., & Kong, X. 2020, *PASP*, 132, 024101, doi: [10.1088/1538-3873/ab6151](https://doi.org/10.1088/1538-3873/ab6151)

Golse, G., & Kneib, J. P. 2002, *A&A*, 390, 821, doi: [10.1051/0004-6361:20020639](https://doi.org/10.1051/0004-6361:20020639)

Goodfellow, I., Bengio, Y., & Courville, A. 2016, Deep Learning (Cambridge, MA: MIT Press)

Grillo, C., Suyu, S. H., Rosati, P., et al. 2015, *ApJ*, 800, 38, doi: [10.1088/0004-637X/800/1/38](https://doi.org/10.1088/0004-637X/800/1/38)

Grogin, N. A., & Narayan, R. 1996, *ApJ*, 464, 92, doi: [10.1086/177302](https://doi.org/10.1086/177302)

He, K., Zhang, X., Ren, S., & Sun, J. 2015, Deep Residual Learning for Image Recognition. <https://arxiv.org/abs/1512.03385>

Horesh, A., Ofek, E. O., Maoz, D., et al. 2005, *ApJ*, 633, 768, doi: [10.1086/466519](https://doi.org/10.1086/466519)

Houlsby, N., Huszár, F., Ghahramani, Z., & Lengyel, M. 2011, arXiv e-prints, arXiv:1112.5745, doi: [10.48550/arXiv.1112.5745](https://doi.org/10.48550/arXiv.1112.5745)

Huang, X., Storfer, C., Ravi, V., et al. 2020, *The Astrophysical Journal*, 894, 78, doi: [10.3847/1538-4357/ab7ffb](https://doi.org/10.3847/1538-4357/ab7ffb)

Huang, X., Storfer, C., Gu, A., et al. 2021, *ApJ*, 909, 27, doi: [10.3847/1538-4357/abd62b](https://doi.org/10.3847/1538-4357/abd62b)

Ioffe, S., & Szegedy, C. 2015, arXiv e-prints, arXiv:1502.03167, doi: [10.48550/arXiv.1502.03167](https://doi.org/10.48550/arXiv.1502.03167)

Ivezić, Ž., Kahn, S. M., Tyson, J. A., et al. 2019, *ApJ*, 873, 111, doi: [10.3847/1538-4357/ab042c](https://doi.org/10.3847/1538-4357/ab042c)

Jacobs, C., Collett, T., Glazebrook, K., et al. 2019, *ApJS*, 243, 17, doi: [10.3847/1538-4365/ab26b6](https://doi.org/10.3847/1538-4365/ab26b6)

Jaelani, A. T., More, A., Wong, K. C., et al. 2024, *MNRAS*, 535, 1625, doi: [10.1093/mnras/stae2442](https://doi.org/10.1093/mnras/stae2442)

Jauzac, M., Richard, J., Jullo, E., et al. 2015, *MNRAS*, 452, 1437, doi: [10.1093/mnras/stv1402](https://doi.org/10.1093/mnras/stv1402)

Jullo, E., & Kneib, J. P. 2009, *MNRAS*, 395, 1319, doi: [10.1111/j.1365-2966.2009.14654.x](https://doi.org/10.1111/j.1365-2966.2009.14654.x)

Jullo, E., Kneib, J. P., Limousin, M., et al. 2007, *New Journal of Physics*, 9, 447, doi: [10.1088/1367-2630/9/12/447](https://doi.org/10.1088/1367-2630/9/12/447)

Jullo, E., Natarajan, P., Kneib, J. P., et al. 2010, *Science*, 329, 924, doi: [10.1126/science.1185759](https://doi.org/10.1126/science.1185759)

Kelly, P. L., Diego, J. M., Rodney, S., et al. 2018, *Nature Astronomy*, 2, 334, doi: [10.1038/s41550-018-0430-3](https://doi.org/10.1038/s41550-018-0430-3)

Khullar, G., Gozman, K., Lin, J. J., et al. 2021, *ApJ*, 906, 107, doi: [10.3847/1538-4357/abcb86](https://doi.org/10.3847/1538-4357/abcb86)

Kingma, D. P., & Ba, J. 2017, Adam: A Method for Stochastic Optimization. <https://arxiv.org/abs/1412.6980>

Kneib, J.-P., Ellis, R. S., Santos, M. R., & Richard, J. 2004, *ApJ*, 607, 697, doi: [10.1086/386281](https://doi.org/10.1086/386281)

Kneib, J. P., Ellis, R. S., Smail, I., Couch, W. J., & Sharples, R. M. 1996, *ApJ*, 471, 643, doi: [10.1086/177995](https://doi.org/10.1086/177995)

Kneib, J. P., Mellier, Y., Fort, B., & Mathez, G. 1993, *A&A*, 273, 367

Kneib, J.-P., & Natarajan, P. 2011, *A&A Rv*, 19, 47, doi: [10.1007/s00159-011-0047-3](https://doi.org/10.1007/s00159-011-0047-3)

Lang, D., Hogg, D. W., & Schlegel, D. J. 2016, *AJ*, 151, 36, doi: [10.3847/0004-6256/151/2/36](https://doi.org/10.3847/0004-6256/151/2/36)

Lanusse, F., Ma, Q., Li, N., et al. 2018, *MNRAS*, 473, 3895, doi: [10.1093/mnras/stx1665](https://doi.org/10.1093/mnras/stx1665)

Lenzen, F., Schindler, S., & Scherzer, O. 2004, *A&A*, 416, 391, doi: [10.1051/0004-6361:20034619](https://doi.org/10.1051/0004-6361:20034619)

Li, R., Napolitano, N. R., Spinelli, C., et al. 2021, *ApJ*, 923, 16, doi: [10.3847/1538-4357/ac2df0](https://doi.org/10.3847/1538-4357/ac2df0)

Liu, Z., Mao, H., Wu, C.-Y., et al. 2022, A ConvNet for the 2020s. <https://arxiv.org/abs/2201.03545>

Massey, R., Kitching, T., & Richard, J. 2010, *Reports on Progress in Physics*, 73, 086901, doi: [10.1088/0034-4885/73/8/086901](https://doi.org/10.1088/0034-4885/73/8/086901)

McInnes, L., Healy, J., & Melville, J. 2020, UMAP: Uniform Manifold Approximation and Projection for Dimension Reduction. <https://arxiv.org/abs/1802.03426>

Meisner, A. M., Lang, D., Schlaftly, E. F., & Schlegel, D. J. 2019, PASP, 131, 124504, doi: [10.1088/1538-3873/ab3df4](https://doi.org/10.1088/1538-3873/ab3df4)

Meneghetti, M., Davoli, G., Bergamini, P., et al. 2020, Science, 369, 1347, doi: [10.1126/science.aax5164](https://doi.org/10.1126/science.aax5164)

Merten, J., Meneghetti, M., Postman, M., et al. 2015, ApJ, 806, 4, doi: [10.1088/0004-637X/806/1/4](https://doi.org/10.1088/0004-637X/806/1/4)

Metcalf, R. B., Meneghetti, M., Avestruz, C., et al. 2019, A&A, 625, A119, doi: [10.1051/0004-6361/201832797](https://doi.org/10.1051/0004-6361/201832797)

Mork, S. D., Gladders, M. D., Khullar, G., et al. 2025, ApJ, 979, 184, doi: [10.3847/1538-4357/ada24c](https://doi.org/10.3847/1538-4357/ada24c)

Nagam, B. C., Acevedo Barroso, J. A., Wilde, J., et al. 2025, A&A, 702, A130, doi: [10.1051/0004-6361/202554132](https://doi.org/10.1051/0004-6361/202554132)

Nair, V., & Hinton, G. E. 2010, in Proceedings of the 27th International Conference on Machine Learning (ICML), 807–814

Narayan, R., & Bartelmann, M. 1996, arXiv e-prints, astro, doi: [10.48550/arXiv.astro-ph/9606001](https://doi.org/10.48550/arXiv.astro-ph/9606001)

Narayan, R., Blandford, R., & Nityananda, R. 1984, Nature, 310, 112, doi: [10.1038/310112a0](https://doi.org/10.1038/310112a0)

Narayan, R., & White, S. D. M. 1988, MNRAS, 231, 97p, doi: [10.1093/mnras/231.1.97P](https://doi.org/10.1093/mnras/231.1.97P)

Navarro, J. F., Frenk, C. S., & White, S. D. M. 1996, ApJ, 462, 563, doi: [10.1086/177173](https://doi.org/10.1086/177173)

Oguri, M. 2010, PASJ, 62, 1017, doi: [10.1093/pasj/62.4.1017](https://doi.org/10.1093/pasj/62.4.1017)

Palencia, J. M., Diego, J. M., Kavanagh, B. J., & Martínez-Arrizabalaga, J. 2024, A&A, 687, A81, doi: [10.1051/0004-6361/202347492](https://doi.org/10.1051/0004-6361/202347492)

Parlange, R., Cuevas-Tello, J. C., Valenzuela, O., et al. 2025, MNRAS, doi: [10.1093/mnras/staf1747](https://doi.org/10.1093/mnras/staf1747)

Petrillo, C. E., Tortora, C., Chatterjee, S., et al. 2017, MNRAS, 472, 1129, doi: [10.1093/mnras/stx2052](https://doi.org/10.1093/mnras/stx2052)

Petrillo, C. E., Tortora, C., Vernardos, G., et al. 2019, MNRAS, 484, 3879, doi: [10.1093/mnras/stz189](https://doi.org/10.1093/mnras/stz189)

Postman, M., Coe, D., Benítez, N., et al. 2012, ApJS, 199, 25, doi: [10.1088/0067-0049/199/2/25](https://doi.org/10.1088/0067-0049/199/2/25)

Refsdal, S. 1964, MNRAS, 128, 307, doi: [10.1093/mnras/128.4.307](https://doi.org/10.1093/mnras/128.4.307)

Richard, J., Smith, G. P., Kneib, J.-P., et al. 2010, MNRAS, 404, 325, doi: [10.1111/j.1365-2966.2009.16274.x](https://doi.org/10.1111/j.1365-2966.2009.16274.x)

Rodriguez, A., & Laio, A. 2014, Science, 344, 1492, doi: [10.1126/science.1242072](https://doi.org/10.1126/science.1242072)

Seidel, G., & Bartelmann, M. 2007, A&A, 472, 341, doi: [10.1051/0004-6361:20066097](https://doi.org/10.1051/0004-6361:20066097)

Silva, D. R., Blum, R. D., Allen, L., et al. 2016, in American Astronomical Society Meeting Abstracts, Vol. 228, American Astronomical Society Meeting Abstracts #228, 317.02

Storfer, C., Huang, X., Gu, A., et al. 2024, ApJS, 274, 16, doi: [10.3847/1538-4365/ad527e](https://doi.org/10.3847/1538-4365/ad527e)

Suyu, S. H., Bonvin, V., Courbin, F., et al. 2017, MNRAS, 468, 2590, doi: [10.1093/mnras/stx483](https://doi.org/10.1093/mnras/stx483)

Tan, M., & Le, Q. V. 2020, EfficientNet: Rethinking Model Scaling for Convolutional Neural Networks. <https://arxiv.org/abs/1905.11946>

Treu, T. 2010, ARA&A, 48, 87, doi: [10.1146/annurev-astro-081309-130924](https://doi.org/10.1146/annurev-astro-081309-130924)

Welch, B., Coe, D., Diego, J. M., et al. 2022, Nature, 603, 815, doi: [10.1038/s41586-022-04449-y](https://doi.org/10.1038/s41586-022-04449-y)

Wong, K. C., Suyu, S. H., Chen, G. C. F., et al. 2020, MNRAS, 498, 1420, doi: [10.1093/mnras/stz3094](https://doi.org/10.1093/mnras/stz3094)

Xu, B., Postman, M., Meneghetti, M., et al. 2016, ApJ, 817, 85, doi: [10.3847/0004-637X/817/2/85](https://doi.org/10.3847/0004-637X/817/2/85)

Xu, D., Zhu, L., Grand, R., et al. 2019, Monthly Notices of the Royal Astronomical Society, 489, 842–854, doi: [10.1093/mnras/stz2164](https://doi.org/10.1093/mnras/stz2164)

Yang, J., Li, N., He, Z., et al. 2025, PASP, 137, 064504, doi: [10.1088/1538-3873/ade400](https://doi.org/10.1088/1538-3873/ade400)

Yue, M., Fan, X., Yang, J., & Wang, F. 2022, AJ, 163, 139, doi: [10.3847/1538-3881/ac4cb0](https://doi.org/10.3847/1538-3881/ac4cb0)

Zou, H., Gao, J., Zhou, X., & Kong, X. 2019, The Astrophysical Journal Supplement Series, 242, 8, doi: [10.3847/1538-4365/ab1847](https://doi.org/10.3847/1538-4365/ab1847)

Zou, H., Zhou, X., Fan, X., et al. 2017, PASP, 129, 064101, doi: [10.1088/1538-3873/aa65ba](https://doi.org/10.1088/1538-3873/aa65ba)

Zou, H., Gao, J., Xu, X., et al. 2021, The Astrophysical Journal Supplement Series, 253, 56, doi: [10.3847/1538-4365/abe5b0](https://doi.org/10.3847/1538-4365/abe5b0)